https://doi.org/10.2352/ISSN.2470-1173.2021.15.COIMG-293

Reducing motion artifact in sequential-scan dual-energy CT imaging by incorporating deformable registration within joint statistical image reconstruction

Tao Ge[1], Rui Liao[1], David G. Politte[2], Maria Medrano[1], Jeffrey F. Williamson[3], Bruce R. Whiting[4], Tianyu Zhao[3], Joseph A. O'Sullivan[1];
[1]Department of Electrical & Systems Engineering, Washington University in St. Louis, St. Louis, MO;
[2]Mallinckrodt Institute of Radiology, Washington University in St. Louis, St. Louis, MO;
[3]Department of Radiation Oncology, Washington University in St. Louis, St. Louis, MO;
[4]Department of Radiology, University of Pittsburgh, Pittsburgh, PA;

Abstract

Dual-energy computed tomography (DECT) has been widely used to reconstruct basis components. In previous studies, our DECT algorithm has shown high accuracy in stopping power ratio (SPR) estimation of fixed objects for proton radiotherapy planning. However, patient movement between sequential data acquisitions may lead to severe motion artifacts in the component images. In order to reduce or eliminate the motion artifacts in clinical applications, we combine a deformable registration method with an accurate joint statistical iterative reconstruction algorithm, dual-energy alternating minimization (DEAM). Image registration is a process of geometrically aligning two or more images. We implement a multi-modality symmetric deformable registration method based on Advanced Normalization Tools (ANTs) to automatically align the scans we acquire for the same patient. The precalculated registration mapping and its inverse are then embedded into each iteration of the DEAM algorithm. The performance of warped DEAM is quantitatively assessed. Theoretically, the performance of warped DEAM on moved patients should be comparable to the performance of the original DEAM algorithm on fixed objects. The warped DEAM algorithm reduces motion artifacts while preserving the accuracy of the iterative joint statistical CT reconstruction algorithm, which enables us to reconstruct accurate results from sequentially scanned dual-energy patient data.

Introduction

Compared to conventional single-energy CT, Dual-energy CT (DECT) generates more informative and quantitative results, such as virtual monoenergetic images, material decomposition images, or electron density maps, from transmission sinograms acquired at two different energies [1]. As a result, DECT has been developed for estimating the proton stopping power ratio (SPR) to reduce estimation uncertainty. The current clinical practice estimates the SPR mappings from the single-energy CT (SECT) results, which leads to $2-3.5\%$ proton beam range uncertainty. We use basis components reconstructed by DECT to estimate proton stopping power for proton radiotherapy planning. Previous studies have shown that our iterative DECT algorithm, dual-energy alternating minimization (DEAM), has achieved sub-percentage uncertainty in estimating proton stopping-power mappings from experimental 3 mm collimated phantom data [2, 3].

Single source sequential acquisition is used when dual energy equipment is not available in the clinic. However, this acquisition method is more vulnerable to object movement, since tens of seconds might elapse between the two scans. In clinical use, voluntary or involuntary movement of the patient may influence the quantitative accuracy of the result and produce severe motion artifacts. A pair of precalculated registration mappings are incorporated into DEAM algorithm in order to reduce motion artifacts.

Deformable image registration has been incorporated with many medical imaging techniques to reconstruct dual-energy images for decades. G. J. Gang et al. utilized deformable registration that aligns two images scanned at different energies before dual-energy decomposition to generate dual-energy x-ray results [4]. It has also been shown that the commercial analytic CT reconstruction techniques with deformable image registration achieved anticipated performances in reconstructing sequentially scanned DECT images. Jessie Huang et al. evaluated the performance of the registration algorithm implemented in Siemens Healthineers SOMATOM Definition Edge scanner on DECT processing [5]. Leng et al. compared the performance of sequentially scanned DECT with Siemens Healthcare Syngo VA 44 and deformable image registration to the dual-source DECT w.r.t differentiating uric acid and non-uric-acid renal stones [6]. To the best of our knowledge, this is the first time that the deformable registration is embedded in an iterative joint statistical DECT algorithm.

Our goal is to incorporate a 3D registration method into an iterative DECT algorithm in order to reduce motion artifacts of patients while preserving the sub-percentage uncertainty in estimating proton stopping-power mappings. The performance of the proposed algorithm on moved patients should be quantitatively comparable to the performance of the original DEAM algorithm on fixed objects.

Methods

DEAM

DEAM is a joint statistical iterative algorithm that minimizes the objective function given by the sum of I-divergence [7],

$$I(d||g) = \sum_j d_j(y) \ln \frac{d_j(y)}{g_j(y:c)} - d_j(y) + g_j(y:c), \qquad (1)$$

and a penalty term,

$$R(c) = \lambda \sum_{i=1}^{2} \sum_{x} \sum_{\tilde{x} \in N_x} w(x,\tilde{x}) \varphi\left(c_i(x) - c_i(\tilde{x})\right), \tag{2}$$

$$\varphi(t) = \delta^2 \left(\left| \frac{t}{\delta} \right| + \log\left(1 - \left| \frac{t}{\delta} \right| \right) \right), \tag{3}$$

where x, y denote the indices of the discretized image space and measurement space, respectively. N_x denotes the set of the neighbouring voxels of the image index x, $w(x,\tilde{x})$ is the voxel weight calculated as the inverse physical distance between voxel x and $\tilde{x}$, λ and δ are two hyper-parameters that control the weight and sparsity of the regularization term, i denotes image component index (specifically 1 for polystyrene and 2 for CaCl2), j denotes measured data index (specifically 1 for 90 kVp and 2 for 140 kVp), d denotes measured data, $g(y:c)$ denotes the estimation of measured data based on image components c_i, which is the forward model, written as

$$g_j(y:c) = \sum_E I_{0,j}(y,E) \exp\left(-\sum_x h(x,y) \sum_{i=1}^{2} \mu_i(E) c_i(x) \right), \tag{4}$$

Algorithm 1: DEAM algorithm without registration

Result: c_1, c_2
Initialization: c_1, c_2, d_L, d_H;
while *Not Converge* **do**
  Apply forward-projection:
  for i in $\{1,2\}$ **do**
    $c_i^F(y) = \sum_x h(x,y) c_i(x)$
  end for
  Apply basis vector model:
  for j in $\{1,2\}$ **do**
    $q_j(y,E) = I_{0,j}(y,E) e^{-\sum_i \mu_i(E) c_i^F(y)}$
  end for
  for i in $\{1,2\}$ **do**
    $\tilde{g}_i(y) = \sum_j \sum_E \mu_i(E) q_j(y,E)$
    $\tilde{d}_i(y) = \sum_j \frac{\sum_E \mu_i(E) q_j(y,E) d_j(y)}{\sum_{E'} q_j(y,E')}$
  end for
  Apply back-projection:
  for i in $\{1,2\}$ **do**
    $g_i^B(x) = \sum_y h(x,y) \tilde{g}_i(y)$
    $d_i^B(x) = \sum_y h(x,y) \tilde{d}_i(y)$
  end for
  Update: Solve decoupled objective function using Newton method
  $\sum_j \sum_i \sum_x d_{ij}^B(x) c_{i1}^{new}$
    $\hookrightarrow$ + $g_{ij}^B(x) \frac{1}{Z_i(x)} \exp(Z_i(x)[c_{i1}^{old}(x) - c_{i1}^{new}(x)])$
    $\hookrightarrow$ + $R(c^{k+1})$
end

where $\mu_i(E)$ denotes the attenuation coeffcient of the i^{th} material at energy E, $I_{0,j}$ denotes the photon counts of the j^{th} peak energy in the absence of an object, which contains information of the spectrum and the bowtie filter, and $h(\cdot,\cdot)$ denotes the system operator that represents the helical fan beam CT system.
The DEAM algorithm is shown in Algorithm 1. c^F is the forward-projection of c, g^B is the back-projection of g. In each iteration, the algorithm consists of four parts: forward projection, basis vector model evaluation, back projection and update.

Registration

Image registration is the process of aligning two or more images of the same scene taken at different times, from different viewpoints, or by different sensors [8]. For the two images registration problem, we will denote one image as a fixed image to provide a reference to the other called a moving image. The general registration algorithm will generate an optimal transformation (mapping) that warps the moving image into the fixed image domain.

Based on our need for constantly warping image volumes between two different material domains (c_1 and c_2), a symmetric algorithm is critical to the whole reconstruction process. The symmetric property will guarantee the inverse consistency of the output transformations. Since the patient anatomy may vary during two successive scans, the algorithm should also be stable with large-scale deformation. After careful evaluation of some available methods, we decided to use the Advanced Normalization Tools (ANTs) [9] toolkit to build our registration code. And we will have a brief introduction of the registration algorithm in this part.

The algorithm ANTs use is called the symmetric image normalization method (SyN) [10]. The framework of the SyN algorithm can be described as an optimization process. The optimal transformation (mapping) φ is acquired by minimizing the total energy function E which is given by

$$\varphi = \text{argmin}_\varphi \, E = \text{argmin}_\varphi \{M + w \times R\}, \tag{5}$$

where w is the weight parameter, M is the similarity term and R is the regularization term .

In our dual energy CT case, the similarity term is selected as the minus mutual information (MI) [11], since the attenuation coefficient of the same material varies under different energy. The regularization term R contributes relatively less than the similarity term M to the total energy function, but it guarantees the minimization process within the space of diffeomorphic maps and provides the Euler-Lagrange equations necessary to solve the optimization problem. A series of diffeomorphisms is computed during the registration process that generates a smooth and invertible path that connects the moving and the fixed images. For each pair of patient data sets, we will be able to obtain a pair of composite (Rigid + Deformable) transformations. We will denote the forward mapping (from the moving image space to the fixed image space) as φ and its inverse as φ^{-1}. The forward mapping composed with the inverse mapping should return an approximate identity transformation which is given by

$$\varphi \circ \varphi^{-1} = I, \tag{6}$$

where $\circ$ denotes the composition operator, e.g. $f \circ g = f\big(g(x)\big)$.

However, in practice, we may still confront small inconsistencies between the two transformations. And those small error

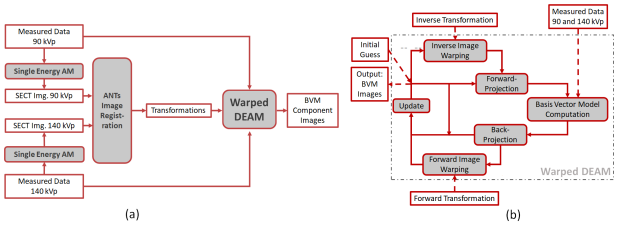

Figure 1. *(a) flowchart of the entire process. (b) flowchart of warped DEAM.*

may accumulate during the iterative reconstruction algorithm and bring some artifacts to the final result. The registration will be executed once per pair of patient scans but the output forward and inverse transformations will be implemented into the loop of the iterative reconstruction algorithm.

Warped DEAM

In order to simulate the image deformation introduced by the patient movement, the registration mapping φ and its inverse φ^{-1} are introduced prior to and after the updating process. The entire process is shown in figure 1(a). Two sequentially scanned measured sinograms are reconstructed individually by the single energy alternating minimization algorithm to get two SECT images. Taking these SECT images, the image registration process will generate the forward and inverse deformation fields.

Suppose the first measured data (scanned at 90 kVp) corresponds to the moving image, and the second measured data (scanned at 140 kVp) corresponds to the fixed image. The flowchart of the warped DEAM algorithm is shown in figure 1(b), and the algorithm is shown in algorithm 2. (c_{1j}, c_{2j}) denotes the basis weights registered to the j^{th} patient position. Compared to the original DEAM, the warped DEAM has two more steps: inverse registration mapping before forward-projection and registration mapping after back-projection. In each iteration, the moving image is registered to the fixed image after the back-projection operation, and the inverse transformation is applied to the relative partial densities c_1 and c_2, respectively, before the forward-projection operation.

Results

Measured data are acquired sequentially on the Phillips Brilliance Big Bore CT scanner located in the Department of Radiation Oncology at the Washington University School of Medicine, scanned at 90 and 140 kVp with 12 mm collimation.

The point-wise mutual information is utilized as the misalignment indicator of two images, which reads

$$PMI_{AB}(x) = p_{AB}\big(A(x),B(x)\big)\log\left(\frac{p_{AB}\big(A(x),B(x)\big)}{p_A\big(A(x)\big)p_B\big(B(x)\big)}\right), \quad (7)$$

where A and B are two target images, x denotes the image index, $P_A(a)$ denotes the probability that value a appears in image A, $P_B(b)$ denotes the probability that value b appears in image B, and $P_{AB}(a,b)$ denotes the probability that value a appears in image A and value b appears in image B. DEAM algorithm is very sensitive to subtle errors, while PMI is pretty good at differentiating little differences if the bin size is properly selected. In this

Algorithm 2: DEAM algorithm with registration (Warped DEAM)

Result: c_{11}, c_{21}
Initialization: c_{11}, c_{21}, d_1, d_2;
while *Not Converged* **do**
Apply inverse registration mapping:
for i in $\{1,2\}$ **do**
$c_{i2} = c_{i1} \circ \varphi^{-1}$
end for
Apply forward-projection:
for i, j in $\{1,2\}$ **do**
$c_{ij}^F(y) = \sum_x h(x,y)c_{ij}(x)$
end for
Apply basis vector model:
for j in $\{1,2\}$ **do**
$q_j(y,E) = I_{0,j}(y,E)e^{-\sum_i \mu_i(E)c_{ij}^F(y)}$
end for
for i, j in $\{1,2\}$ **do**
$\tilde{g}_{ij}(y) = \sum_E \mu_i(E)q_j(y,E)$
$\tilde{d}_{ij}(y) = \frac{\sum_E \mu_i(E)q_j(y,E)d_j(y)}{\sum_{E'} q_j(y,E')}$
end for
Apply back-projection:
for i in $\{1,2\}$ **do**
$g_{i1}^B(x) = \sum_y h(x,y)\tilde{g}_{i1}(y)$
$\tilde{g}_{i2}^B(x) = \sum_y h(x,y)\tilde{g}_{i2}(y)$
$d_{i1}^B(x) = \sum_y h(x,y)\tilde{d}_{i1}(y)$
$\tilde{d}_{i2}^B(x) = \sum_y h(x,y)\tilde{d}_{i2}(y)$
end for
Apply inverse registration mapping:
for i in $\{1,2\}$ **do**
$g_{i2}^B(x) = \tilde{g}_{i2}^B(x) \circ \varphi$
$d_{i2}^B(x) = \tilde{d}_{i2}^B(x) \circ \varphi$
end for
Update: Solve decoupled objective function using Newton method
$\sum_j \sum_i \sum_x \Big[d_{ij}^B(x)c_{i1}^{new} +$
$\hookrightarrow \; g_{ij}^B(x)\frac{1}{Z_i(x)}\exp(Z_i(x)[c_{i1}^{old}(x) - c_{i1}^{new}(x)]) \Big]$
$\hookrightarrow \; + \mathrm{R}(\mathrm{c}^{k+1})$
end

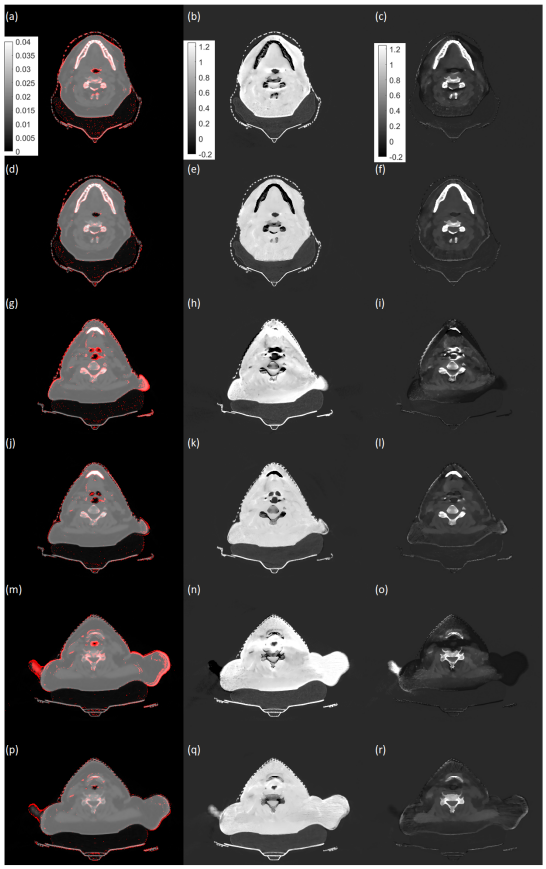

Figure 2. *Comparison between pre-registration and post-registration results. From left to right column: inverse PMI overlaying on corresponding 140 kVp image slice, c_1 from original DEAM, c_2 from original DEAM. First, third and fifth row: slice of pre-registration results in different z-position from the same patient. Second, fourth and sixth row: corresponding slice of pose-registration results in different z-position from the same patient.*

project, the range of the bin is chosen to be [0, 0.04], with the bin number of 32.

Figure 2 shows the pre-registration and post-registration results. From left to right column: inverse PMI overlaying on corresponding 140 kVp image slice, c_1 from original DEAM, c_2 from original DEAM. From figure 2(a-c), slight mismatches could be observed in the throat area, so we see an overestimation of c_1 and an underestimation of c_2 near the throat. More mismatches could be seen in the second slice of pre-registration images figure 2(g-j) around the throat and right shoulder, which leads to more severe artifacts in DECT reconstructed results. The pharyngeal wall and tracheal wall are reconstructed as bone-like high-density structures due to the misalignment. In the third slice of pre-registration figure 2(m-o), the motion artifact on the left shoulder has the same shape as the mismatch indicated by inverse PMI. Moreover, more mismatches appear on the boundary of the right shoulder. The mismatch influences the value of DECT images not only at their corresponding position, but also in the area surrounded by them.

Compared to pre-registration results, post-registration results have fewer mismatches and motion artifacts. For all the selected

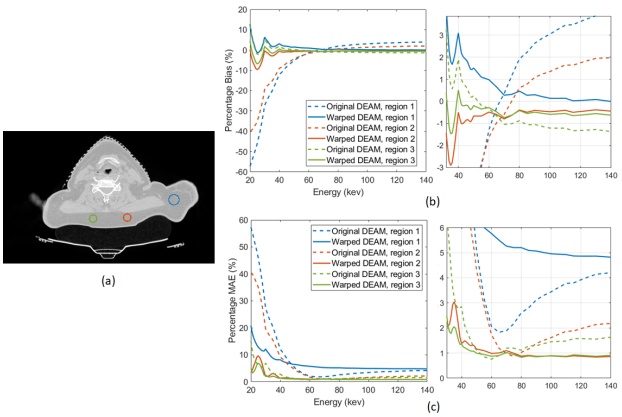

Figure 3. *(a) regions of interest in the adipose are indicated by circles. (b) the plot and the magnified plot of percentage bias vs. energy. (c) the plot and the magnified plot of percentage mean absolute error vs. energy.*

slices, the magnitude and area of inverse PMI are reduced after registration. The algorithm could correctly reconstruct the margins of the throat and trachea as soft tissues rather than bones. Also, by comparing figure 2(q)(r) to figure 2(n)(o), c_1, c_2 of the warped DEAM for the right shoulder now have similar values to other adipose tissues that are not affected by the mismatch. However, in figure 2(p-r), there is still a mismatch on the edge of the right shoulder, which leads to the bone-like artifact in the reconstructed results.

Moreover, we analyze the performance of the warped DEAM algorithm quantitatively. The following quantitative analyses are based on the assumption that the property of the adipose of the object is close to our anticipation. Three regions of interest in the adipose are indicated by circles, shown in figure 3(a). The ROIs are cylinders, but only one slice is shown here for visualization convenience. Figure 3(b) and (c) shows the error of the DEAM result on estimating attenuation coefficients at different energies of the adipose of the object.

As the metrics, percentage bias and mean absolute error (MAE) of estimated attenuations at different energies are calculated by

$$bias = \frac{1}{N}\sum_{x}\frac{c_1(x)\mu_1(E)+c_2(x)\mu_2(E)-\mu_{ref}(E)}{\mu_{ref}(E)}\times 100\% \quad (8)$$

and

$$MAE = \frac{1}{N}\sum_{x}\frac{|c_1(x)\mu_1(E)+c_2(x)\mu_2(E)-\mu_{ref}(E)|}{\mu_{ref}(E)}\times 100\%, \quad (9)$$

respectively, where μ_{ref} are the reference attenuation coefficients of adipose come from [12].

Figure 3(b) shows the plot of the percentage bias versus energy. The warped DEAM has a lower bias than the original DEAM at most of the energies. Biases in region 1 and region 2 are greatly reduced. The values of warped DEAM in region 2 and region 3 are below 1% after 40 kev. The values of warped DEAM in region 1 are below 1% after 60 kev, while most of the values of original DEAM in three regions are greater than 1%.

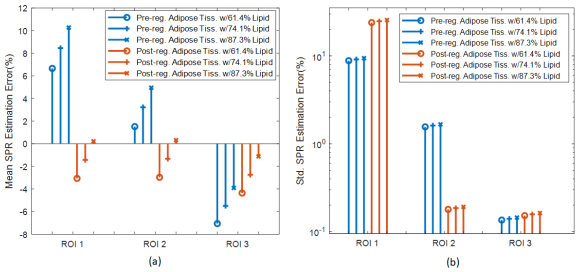

Figure 4. *(a) Mean errors of SPR estimated by original DEAM and warped DEAM. (b) Standard deviation errors of SPR estimated by original DEAM and warped DEAM*

Figure 3(c) shows the plot of the percentage MAE versus energy. MAEs of warped DEAM in region 2 and region 3 are still lower than MAE of original DEAM at most of the energies, and MAE of warped DEAM in region 2 and region 3 vibrate near 1% after 40 kev. However, the MAE of warped DEAM in region 1 is higher than MAE of the original DEAM after 45 kev. We noticed that the warping of images introduces noise in the reconstructed results.

Figure 4 compares the mean and standard deviation error between original DEAM and warped DEAM on SPR estimation. We use adiposes with different percentage of lipid to match the SPR of adipose of the object. Figure 4(a) shows that mean errors of SPR estimated by warped DEAM are smaller than SPR estimated by original DEAM in all regions for all lipid percentages, except for 61.4% percent lipid in region 2. It is worth noticing that the mean errors of the estimated SPR to the reference adipose SPR with 87.3% lipid are below $\pm 1\%$ in all the selected ROIs.

Figure 4(b) shows that standard deviation errors of SPR estimated by warped DEAM are below 1% in region 2 and 3 for all lipid percentages. The standard deviation error of SPR estimated by original DEAM is also below 1% in region 3 because this region was hardly affected by the mismatch. However, in region 1, the standard deviation errors of both results are around 10%, and the warped DEAM is worse than the original DEAM because of the noise introduced by the warping process.

Conclusion

We proposed an iterative DECT reconstruction algorithm with embedded deformable registration mapping that could reduce motion artifacts. We visually compared the performance of the warped DEAM and original DEAM, and quantitatively assess the image quality w.r.t mono-energy and SPR estimation. It has been shown that the warped DEAM outperformed the original DEAM in reconstructing sequentially scanned deformed DECT data.

Acknowledgments

This study is supported by NIH R01 CA 212638.

References

[1] Yu L Fletcher JG. McCollough CH, Leng S. Dual- and multi-energy ct: principles, technical approaches, and clinical applications. *Radiology*, 276:637–653, 2015.

[2] Shuangyue Zhang, Dong Han, Jeffrey F. Williamson, Tianyu Zhao, David G. Politte, Bruce R. Whiting, and Joseph A. O'Sullivan. Experimental implementation of a joint statistical image reconstruction method for proton stopping power mapping from dual-energy ct data. *Medical Physics*, 46(1):273–285, 2019.

[3] Maria Medrano, Ruirui Liu, Tyler Webb, Tianyu Zhao, Jeffrey Williamson, Bruce Whiting, David G. Politte, Mariela Porras-Chaverri, and Joseph A. O'Sullivan. Accurate proton stopping power images reconstructed using joint statistical dual energy CT: experimental verification and impact of fan-beam CT scatter. In Guang-Hong Chen and Hilde Bosmans, editors, *Medical Imaging 2020: Physics of Medical Imaging*, volume 11312, pages 430 – 438. International Society for Optics and Photonics, SPIE, 2020.

[4] G. J. Gang, C. A. Varon, H. Kashani, S. Richard, N. S. Paul, R. Van Metter, J. Yorkston, and J. H. Siewerdsen. Multiscale deformable registration for dual-energy x-ray imaging. *Medical Physics*, 36(2):351–363, 2009.

[5] Jessie Y. Huang, Michael J. Lawless, Charles K. Matrosic, Lianna D. Di Maso, and Jessica R. Miller. Evaluation of a commercial deformable image registration algorithm for dual-energy ct processing. *Journal of Applied Clinical Medical Physics*, 21(9):227–234, 2020.

[6] Ai S et al Leng S, Shiung M. Feasibility of discriminating uric acid from non-uric acid renal stones using consecutive spatially registered low- and high-energy scans obtained on a conventional ct scanner. *AJR*, 204:92–97, 2015.

[7] J. A. O'Sullivan and J. Benac. Alternating minimization algorithms for transmission tomography. *IEEE Transactions on Medical Imaging*, 26(3):283–297, 2007.

[8] Barbara Zitova and Jan Flusser. Image registration methods: a survey. *Image and vision computing*, 21(11):977–1000, 2003.

[9] Brian B Avants, Nick Tustison, and Gang Song. Advanced normalization tools (ants). *Insight j*, 2(365):1–35, 2009.

[10] Brian B Avants, Charles L Epstein, Murray Grossman, and James C Gee. Symmetric diffeomorphic image registration with cross-correlation: evaluating automated labeling of elderly and neurodegenerative brain. *Medical image analysis*, 12(1):26–41, 2008.

[11] Frederik Maes, Andre Collignon, Dirk Vandermeulen, Guy Marchal, and Paul Suetens. Multimodality image registration by maximization of mutual information. *IEEE transactions on Medical Imaging*, 16(2):187–198, 1997.

[12] Aysun Böke. Linear attenuation coefficients of tissues from 1 keV to 150 keV. *Radiation Physics and Chemistry*, 102:49–59, September 2014.

Author Biography

Tao Ge received his BS in electrical & information engineering from Harbin Engineering University (2016) and his MS in electrical engineering from Washington University in St. Louis (2018). He is currently a Ph.D. candidate in electrical engineering at Washington University in St. Louis. His work has focused on the acceleration and optimization of the accurate dual energy CT algorithm.

Rui Liao received his BS in automation from Beihang University (2017) and his MS in electrical engineering from Washington University in St. Louis (2019). He is currently a Ph.D. candidate in image science program at Washington University in St. Louis. His work has focused on the medical image registration.

JOIN US AT THE NEXT EI!

IS&T International Symposium on

Electronic Imaging

SCIENCE AND TECHNOLOGY

Imaging across applications . . . Where industry and academia meet!

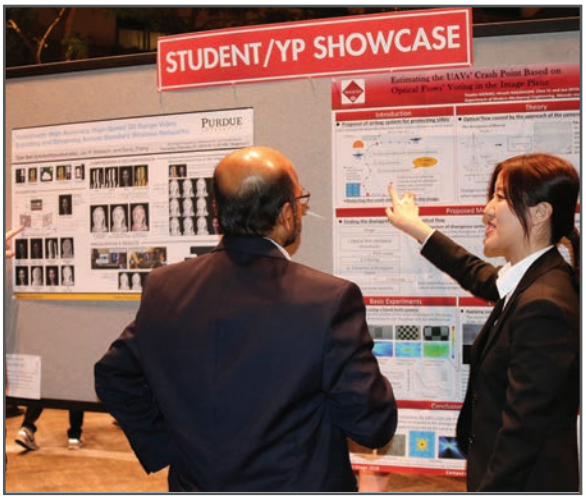

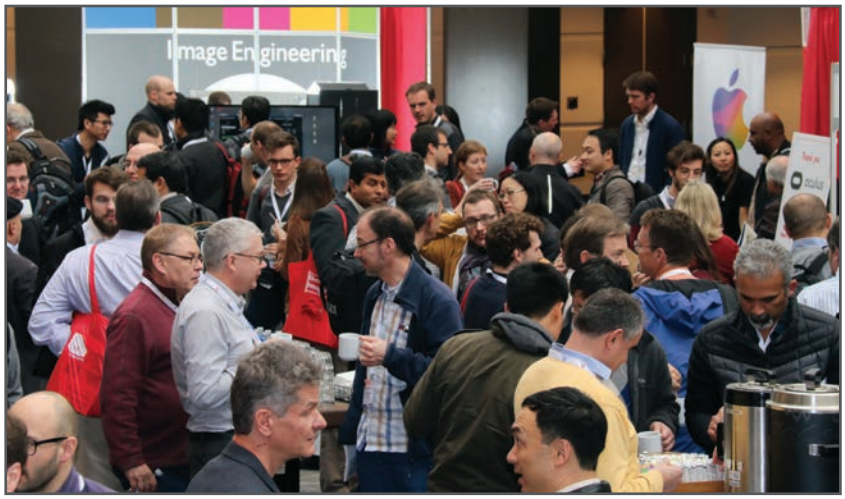

• SHORT COURSES • EXHIBITS • DEMONSTRATION SESSION • PLENARY TALKS •
• INTERACTIVE PAPER SESSION • SPECIAL EVENTS • TECHNICAL SESSIONS •

www.electronicimaging.org

IS&T
imaging.org